Monthly Notices of the ROYAL ASTRONOMICAL SOCIETY

MNRAS **444,** 2870–2883 (2014) doi:10.1093/mnras/stu1569

HerMES: point source catalogues from *Herschel*-SPIRE observations II★

L. Wang,[1,2]† M. Viero,[3] C. Clarke,[1] J. Bock,[3,4] V. Buat,[5] A. Conley,[6] D. Farrah,[1,7] K. Guo,[1,8] S. Heinis,[5] G. Magdis,[9] L. Marchetti,[10,11] G. Marsden,[12] P. Norberg,[2] S. J. Oliver,[1] M. J. Page,[13] Y. Roehlly,[5] I. G. Roseboom,[1,14] B. Schulz,[3,15] A. J. Smith,[1] M. Vaccari[9,16] and M. Zemcov[3,4]

[1]*Astronomy Centre, Department of Physics and Astronomy, University of Sussex, Brighton BN1 9QH, UK*
[2]*Department of Physics, Institute for Computational Cosmology, Durham University, South Road, Durham DH1 3LE, UK*
[3]*California Institute of Technology, 1200 E. California Blvd, Pasadena, CA 91125, USA*
[4]*Jet Propulsion Laboratory, 4800 Oak Grove Drive, Pasadena, CA 91109, USA*
[5]*Laboratoire d'Astrophysique de Marseille, OAMP, Université Aix-marseille, CNRS, 38 rue Frédéric Joliot-Curie, F-13388 Marseille cedex 13, France*
[6]*Center for Astrophysics and Space Astronomy, 389-UCB, University of Colorado, Boulder, CO 80309, USA*
[7]*Department of Physics, Virginia Tech, Blacksburg, VA 24061, USA*
[8]*Purple Mountain Observatory, Chinese Academy of Sciences, 2 West-Beijing Road, Nanjing 210008, China*
[9]*Denys Wilkinson Building, Keble Road, University of Oxford, Oxford OX1 3RH, UK*
[10]*Dipartimento di Astronomia, Università di Padova, vicolo Osservatorio, 3, I-35122 Padova, Italy*
[11]*Department of Physical Sciences, The Open University, Milton Keynes MK7 6AA, UK*
[12]*Department of Physics and Astronomy, University of British Columbia, 6224 Agricultural Road, Vancouver, BC V6T 1Z1, Canada*
[13]*Mullard Space Science Laboratory, University College London, Holmbury St Mary, Dorking, Surrey RH5 6NT, UK*
[14]*Institute for Astronomy, University of Edinburgh, Royal Observatory, Blackford Hill, Edinburgh EH9 3HJ, UK*
[15]*Infrared Processing and Analysis Center, MS 100-22, California Institute of Technology, JPL, Pasadena, CA 91125, USA*
[16]*Astrophysics Group, Physics Department, University of the Western Cape, Private Bag X17, Bellville, Cape Town 7535, South Africa*

Accepted 2014 August 1. Received 2014 August 1; in original form 2013 December 12

ABSTRACT

The *Herschel* Multi-tiered Extragalactic Survey (HerMES) is the largest Guaranteed Time Key Programme on the *Herschel* Space Observatory. With a wedding cake survey strategy, it consists of nested fields with varying depth and area totalling ∼380 deg^2. In this paper, we present deep point source catalogues extracted from *Herschel*-Spectral and Photometric Imaging Receiver (SPIRE) observations of all HerMES fields, except for the later addition of the 270 deg^2 HerMES Large-Mode Survey (HeLMS) field. These catalogues constitute the second Data Release (DR2) made in 2013 October. A sub-set of these catalogues, which consists of bright sources extracted from *Herschel*-SPIRE observations completed by 2010 May 1 (covering ∼74 deg^2) were released earlier in the first extensive data release in 2012 March. Two different methods are used to generate the point source catalogues, the SUSSEXTRACTOR point source extractor used in two earlier data releases (EDR and EDR2) and a new source detection and photometry method. The latter combines an iterative source detection algorithm, STARFINDER, and a De-blended SPIRE Photometry algorithm. We use end-to-end *Herschel*-SPIRE simulations with realistic number counts and clustering properties to characterize basic properties of the point source catalogues, such as the completeness, reliability, photometric and positional accuracy. Over 500 000 catalogue entries in HerMES fields (except HeLMS) are released to the public through the HeDAM (*Herschel* Database in Marseille) website (http://hedam.lam.fr/HerMES).

Key words: methods: statistical – techniques: photometric – catalogues – surveys – infrared: galaxies – submillimetre: galaxies.

1 INTRODUCTION

The *Herschel* Multi-tiered Extragalactic Survey (HerMES[1]; Oliver et al. 2012) is a Guaranteed Time Key Programme on the *Herschel*

★Herschel is an ESA space observatory with science instruments provided by European-led Principal Investigator consortia and with important participation from NASA.

†E-mail: lingyu.wang25@gmail.com

[1] http://hermes.sussex.ac.uk

Table 1. Summary of the HerMES observations released in DR1. The columns are the set identification number, the design level, the target name, the observing mode, the area of good pixels $\Omega_{\rm good}$, where the number of bolometer samples per pixel in the 250 μm map is greater than half of the median value, and the 5σ instrumental noise level at 250, 350 and 500 μm.

Set	Level	Target	Mode	$\Omega_{\rm good}$ (deg^2)	$5\sigma^{\rm ins.}_{250}$ (mJy)	$5\sigma^{\rm ins.}_{350}$ (mJy)	$5\sigma^{\rm ins.}_{500}$ (mJy)
1	CD	Abell 2218	Sp. Nom.	0.10	6.4	5.3	7.6
3	CD	MS0451.6−0305	Sp. Nom.	0.08	9.2	7.7	11.0
7	CS	Abell 2219	Sp. Nom.	0.08	9.2	7.7	11.0
14	L2	GOODS-N	Sp. Nom.	0.55	3.8	3.1	4.5
15	L2	ECDFS	Sp. Nom.	0.58	4.3	3.6	5.2
17	L3	Groth Strip	Sp. Nom.	0.60	10.7	8.9	12.8
19	L3	Lockman-North	Sp. Nom.	0.65	10.6	8.8	12.7
28	L5	Lockman SWIRE	Sp. Fast	17.37	13.6	11.2	16.2
30	L5	Bootes HerMES	Parallel	3.25	13.8	11.3	16.4
31	L5	ELAIS N1 HerMES	Parallel	3.25	13.8	11.3	16.4
36	L6	XMM-LSS SWIRE	Parallel	18.87	11.2	9.3	13.4
37	L6	Bootes NDWFS	Parallel	10.57	13.8	11.3	16.4
38	L6	ADFS	Parallel	7.47	25.8	21.2	30.8
40	L6	FLS	Parallel	6.71	25.8	21.2	30.8

Space Observatory (Pilbratt et al. 2010). It has a wedding cake survey design which consists of nested fields ranging from shallow and wide fields to deep and narrow fields observed with the *Herschel*-Spectral and Photometric Imaging Receiver (SPIRE; Griffin et al. 2010) at 250, 350 and 500 μm[2] and the *Herschel*-Photodetector Array Camera and Spectrometer (PACS; Poglitsch et al. 2010) at 100 and 160 μm for a sub-set of the HerMES fields. There are 13 target blank fields at approximately seven different depths (Levels 1–7) covering a total area of ∼380 deg^2 which includes a later addition of a wide HerMES Large-Mode Survey (HeLMS) field (270 deg^2) observed by SPIRE alone. In addition to the blank fields, HerMES also targeted 12 known clusters. The first two data releases, Early Data Release (EDR, 2010 July 1) and EDR2 (2011 September 19), included SPIRE high signal-to-noise ratio (SNR $\geq$ 5) sources extracted from HerMES Science Demonstration Phase (SDP[3]) and the first Data Release (DR1) fields (see Table 1) generated by the SUSSEXTRACTOR (SXT) point source extractor (Smith et al. 2012) as well as SPIRE maps in the Abell 2218 cluster field.

This paper describes the generation of HerMES point source catalogues extracted from *Herschel*-SPIRE observations completed by 2010 May 1 and released during the first extensive data release (DR1) of maps and catalogues (2012 March 27) and all observations except HeLMS released during the second extensive data release (DR2; 2013 October 31). All HerMES fields apart from HeLMS (which is not included in DR2) are deliberately chosen to be in relatively cirrus-free regions and therefore avoid issues with false detections associated with cirrus emission. Details of DR1 and DR2 are given in Tables 1 and 2. As catalogues are the starting point for understanding the far-infrared/sub-millimetre (sub-mm) galaxy population in detail (e.g. their spectral energy distributions, redshift distribution and luminosity), a lot of effort has been invested in constructing deep and reliable catalogues. The main challenge is confusion noise which arises when the spatial extent of the emission from distinct sources overlap within the same area, creating signal fluctuations within the telescope beam. At a given wavelength, this will mostly depend on the intrinsic flux density distribution of sources as well as the resolving power and sensitivity of the instrument used for the observations. Nguyen et al. (2010) found that in the limit of infinite integration time (i.e. negligible instrumental noise) the SPIRE confusion noise is at the level of $5\sigma = 24.0, 27.5, 30.5$ mJy at 250, 350 and 500 μm, respectively (after excluding map pixels at $>=5\sigma$). Confusion noise is a significant feature (much larger than instrumental noise) for most of the HerMES fields (from Level 1 to Level 4; see Tables 1 and 2) and sets a fundamental limit on the flux limit of sources that can be detected by a peak finding algorithm such as SXT.

Bright sources that can be resolved individually by *Herschel* only account for a small fraction of the cosmic infrared background (e.g. Oliver et al. 2010; Glenn et al. 2010; Béthermin et al. 2012). To extract deeper catalogues, we must reduce the level of confusion noise in our maps. In this paper, we present a new source detection and photometry method which combines an iterative source detection algorithm STARFINDER (SF) and a De-blended SPIRE Photometry (DESPHOT) algorithm. SF iteratively detects and removes sources to reduce the confusion noise level and therefore can extract sources below the nominal confusion limit. DESPHOT is optimized for accurate photometry in highly confused images.

The paper is organized as follows. In Section 2, first we describe SPIRE observations and the extracted data products of the HerMES fields released in DR1 and DR2. Then, we describe in detail the two different source extraction methods (SXT and SF combined with DESPHOT) used to generate the DR1 and DR2 point sources catalogues. In Section 3, realistic end-to-end *Herschel*-SPIRE simulations are used to understand the basic properties (e.g. photometric and positional error, completeness and reliability) of the point source catalogues. The issue of extended sources being broken up by our source extraction methods is discussed in Section 4. Finally, we give conclusions and discussions in Section 5.

2 HERMES DR1 AND DR2 POINT SOURCE CATALOGUES

2.1 Overview of DR1 and DR2 SPIRE observations and data products

HerMES DR1 includes bright sources (above 55, 55 and 30 mJy at 250, 350 and 500 μm, respectively) extracted from the SDP observations as well as all SPIRE observations completed by 2010

[2] The SPIRE bands at 250, 350 and 500 μm are also known as the SPIRE Photometer Short Wavelength array (PSW), SPIRE Photometer Median Wavelength array (PMW) and SPIRE Photometer Long Wavelength array (PLW), respectively.

[3] The SDP fields include the First Look Survey (FLS), the Great Observatories Origins Deep Survey North field (GOODS-N), Lockman the Spitzer Wide-area InfraRed Extragalactic survey (SWIRE) and Lockman-North.

Table 2. Summary of the additional HerMES observations released in DR2. The columns are the same as in Table 1.

Set	Level	Target	Mode	$\Omega_{\rm good}$ (deg^2)	$5\sigma^{\rm ins.}_{250}$ (mJy)	$5\sigma^{\rm ins.}_{350}$ (mJy)	$5\sigma^{\rm ins.}_{500}$ (mJy)
2	CD	Abell 1689	Sp. Nom.	0.08	9.2	7.7	11.0
4	CS	RXJ13475-1145	Sp. Nom.	0.08	9.2	7.7	11.0
5	CS	Abell 1835	Sp. Nom.	0.08	9.2	7.7	11.0
6	CS	Abell 2390	Sp. Nom.	0.08	9.2	7.7	11.0
8	CS	Abell 370	Sp. Nom.	0.08	9.2	7.7	11.0
9	CS	MS1358 62	Sp. Nom.	0.08	9.2	7.7	11.0
10	CS	Cl0024 16	Sp. Nom.	0.08	9.2	7.7	11.0
11	CH	MS1054.4−0321	Sp. Nom.	0.16	13.9	11.6	16.7
12	CH	RXJ0152.7-1357	Sp. Nom.	0.16	13.9	11.6	16.7
13	L1	GOODS-S	Sp. Nom.	0.35	4.3	3.6	5.2
22	L2	COSMOS	Sp. Nom.	2.82	8.0	6.6	9.5
18	L3	Lockman-East *ROSAT*	Sp. Nom.	0.57	9.6	7.9	11.5
18B	L3	Lockman-East *Spitzer*	Sp. Nom.	1.40	9.6	7.9	11.5
23	L4	UDS	Sp. Nom.	2.02	11.2	9.3	13.4
24	L4	VVDS	Sp. Nom.	2.02	11.2	9.3	13.4
22B	L5	COSMOS HerMES	Sp. Nom.	4.38	15.9	13.3	19.1
27	L5	CDFS SWIRE	Sp. Fast	11.39	12.7	10.5	15.2
28B	L5	Lockman SWIRE	Sp. Fast	7.63	13.6	11.2	16.2
29	L5	EGS HerMES	Parallel	2.67	10.7	8.9	12.8
32	L5	XMM VIDEO1	Parallel	2.72	14.9	12.2	17.8
32B	L5	XMM VIDEO2	Parallel	1.74	14.9	12.2	17.8
32C	L5	XMM VIDEO3	Parallel	2.73	14.9	12.2	17.8
33	L5	CDFS SWIRE	Parallel	10.89	8.0	6.6	9.6
34	L5	Lockman SWIRE	Parallel	16.08	9.6	7.9	11.5
39B	L5	ELAIS S1 VIDEO	Parallel	3.72	14.9	12.2	17.8
35	L6	ELAIS N1 SWIRE	Parallel	12.28	25.8	21.2	30.8
39	L6	ELAIS S1 SWIRE	Parallel	7.86	25.8	21.2	30.8
41	L6	ELAIS N2 SWIRE	Parallel	7.80	25.8	21.2	30.8

May 1. Table 1 gives a summary of the HerMES observations released in DR1, including the set identification number,[4] the design level, the target name, the observing mode (including the nominal SPIRE scan rate at 30 arcsec s^{-1}, the fast SPIRE scan rate at 60 arcsec s^{-1} and the SPIRE–PACS parallel mode), the area of good pixels $\Omega_{\rm good}$, where the number of bolometer samples per pixel in the 250 μm map is greater than half of the median value, and the 5σ instrumental noise level at 250, 350 and 500 μm. HerMES DR2 includes all point sources from the SDP and DR1 fields as well as all subsequent SPIRE observations except HeLMS. Table 2 gives a summary of the additional HerMES fields included in DR2.

The data obtained from the *Herschel* Science Archive were processed with a combination of standard ESA software and a customized software package SMAP. For HerMES DR1 and DR2, raw telescope data were processed into calibrated timelines using HIPE[5] (Ott 2010) version 6.0.3 with the SPIRE calibration tree version spire_cal_6_1, which are relatively old compared to the current versions. The most important photometric update since then is the change of the Neptune radiative model which resulted in changes of a few per cent depending on filter band. In the nominal mode, the flux corrections terms (i.e. ratio of flux densities) are 1.0253, 1.0250 and 1.0125 at 250, 350 and 500 μm, respectively. We recommend users to apply these correction factors to update photometry in the released source catalogues.

Details of the timeline processing steps in HIPE are described in Dowell et al. (2010) and the SPIRE Observers Manual.[6] Briefly, the raw data are converted into detector voltages and then several corrections are made. The corrections include detection and masking of cosmic ray glitches, correction for the electrical filter response, converting signal-to-flux density, temperature drift removal, corrections for bolometer time response and merging with the telescope-pointing product to produce sky coordinates.

SMAP differs from HIPE in three fundamental ways. First, the standard scan-by-scan temperature drift correction module within HIPE is overridden in favour of a custom correction algorithm which stitches together all of the time-ordered data (or time streams), allowing us to fit to and remove a much longer noise mode. Further, the standard processing is modified such that a 'sigma–kappa' deglitcher is used instead of a wavelet deglitcher, to improve performance in large blank fields. Lastly, imperfections from thermistor jumps, the 'cooler burp' effect and residual glitches are removed manually before map construction.

HerMES maps are created by the SMAP map-maker, SHIM (SPIRE-HerMES Iterative Mapper), iteratively removes a low-order polynomial baseline from each scan.[7] At each iteration i, a

[4] The set identification number is defined in Oliver et al. (2012). Observations of the same field at the same level made with the same mode and areal size are grouped into a 'set'.

[5] The Herschel Interactive Processing Environment (HIPE) is the application developed by ESA that allows users to work with the *Herschel* data, including finding the data products, interactive analysis, plotting of data and data manipulation. See http://herschel.esac.esa.int/hipe/

[6] http://herschel.esac.esa.int/Docs/SPIRE/html/spire_handbook.html

[7] The removal of a low-order polynomial baseline removes some but not all of the foreground cirrus emission. In theory, the source identification code could first high-pass filter the map in Fourier space to remove cirrus and other large-scale power. In fact, this is done in HeLMS with severe cirrus contamination. However, the problem with high-pass filter is that the large-scale clustering power of the point sources will be suppressed as a result.

polynomial is fitted to the time-stream residual $R_i = S - M_{i-1}$, where S is the time stream and M_{i-1} is the predicted time stream given the map calculated on the previous iteration. Additionally, each scan is given a weight based on the inverse variance of the time-stream residual. The order or the polynomial baseline varies from 0 to 2, depending on the size of the map. These maps are made with 20 iterations, which appear to provide sufficient convergence. The algorithm is fully described in Levenson et al. (2010) and Viero et al. (2013).

We provide three different types of point source catalogues extracted from the SMAP v4.1 maps as follows.

(i) Independent single-band SXT catalogues at 250, 350 and 500 μm. SXT is used to detect point sources and estimate their positions and fluxes.

(ii) Independent single-band SF catalogues with DESPHOT photometry at 250, 350 and 500 μm. SF is used to detect sources and find their optimal positions, while DESPHOT is used to estimate fluxes for a given list of source positions. For convenience, we will refer to these catalogues as SF catalogues.

(iii) Band-merged SF catalogues with DESPHOT multiband (250, 350 and 500 μm) photometry at the positions of the SF 250 μm sources. We will refer to these catalogues as SF250 catalogues.

The source extraction algorithms, i.e. SXT and SF, as well as our custom-made photometry code DESPHOT are described in detail in Sections 2.2 and 2.3. The point source catalogues can be downloaded from the *Herschel* Database in Marseille [HeDaM (Roehlly et al. 2011); http://hedam.lam.fr/HerMES]. Apart from the SF250 catalogues, sources are directly detected in the image where we want to perform photometry, with no additional information obtained from other wavelengths. As a result, it allows detection of sources which might be unidentified at other wavelengths. However, when source density is too high, blind source extraction cannot separate blended point sources. The source centroid from blind source catalogues might be less well constrained causing greater difficulty in cross-matching sources detected at different wavelengths. Admittedly, source extraction with prior information (e.g. from deep 24 μm observations) on the spatial distribution of sources in the sky (Roseboom et al. 2010, 2012) will in general provide deeper catalogues and more robust source identification across different wavelengths. But it can risk misidentifying sources with positive noise fluctuations, if we assume that all sources in the prior model have a counterpart in the SPIRE maps.

SPIRE calibration is done by fitting the point spread function to the time-stream signal of Neptune. The measurement is repeatable at 2 per cent level and the quoted uncertainty of the Neptune model is 5 per cent. As a result, the calibration uncertainty is 7 per cent.

2.2 SXT versus SF

SXT is a peak finding algorithm (implemented in JAVA within HIPE optimized for isolated sources. For the sake of completeness, we briefly summarize the SXT source extraction algorithm here.

(i) First, the image is smoothed with a Gaussian point response function (PRF), with the pixels weighted according to the noise level in the map.

(ii) The PRF-filtered image is then searched for local maxima. A local maximum is a pixel which is higher than all of its immediate neighbours (i.e. the eight pixels surrounding it). Pixels close to the edge of the image are ignored.

(iii) The position of the local maximum is refined by fitting a quadratic function to certain pixels in the PRF-filtered image. This gives the source position to a better accuracy than simply the centre of a pixel.

(iv) The PRF-filtered image gives, for each pixel, the maximum likelihood estimate of the flux density of a source centred on the centre of that pixel (with a separate image giving the estimate of the uncertainty in the flux density). However, for sources not located at the centre of a pixel, this would be an underestimate of the flux. Simulations are performed to determine a correction to be applied to all sources, in order to eliminate a systematic bias in the estimates of the flux. (It should be noted that later releases of HIPE contain a version of SXT that does not have this problem.)

(v) Only those sources with a signal-to-noise ratio (SNR) above a specified detection threshold are accepted as detections.

For more details, please refer to Savage & Oliver (2007), Hobson, Rocha & Savage (2010), Smith et al. (2011) and the detailed documentation contained within HIPE.

SF is an iterative source finding and fitting program (implemented in IDL), originally designed for crowded stellar fields analysis (Diolaiti et al. 2000). SF, thus, is expected to do better at de-blending sources and finding faint sources around bright sources. SF models the observed image as a superposition of shifted scaled replicas of the PRF lying on a smooth background. At each iteration, SF performs the following steps.

(i) Detects new sources by searching for local maxima above a given SNR threshold in the image after subtraction of the known sources.

(ii) Cross-correlates each of the sub-images centred at the newly detected sources with the PRF and accepts those with correlation coefficients (a measure of the similarity between the source profile and our template) above a given threshold.

(iii) For each of the accepted new sources, determines the best-fitting position and flux of the source of interest by fitting to the sub-image centred around the source. Adds all of the new sources with the optimal positions and fluxes to the list of accepted sources and repeats from step (i) with a lower SNR threshold.

In both source extraction methods, for computational efficiency, we use a Gaussian-shaped PRF with the full width half-maximum (FWHM) set to 18.15, 25.15 and 36.3 arcsec at 250, 350 and 500 μm, respectively (Swinyard et al. 2010), although the SPIRE beams are known to be significantly elliptical. As our source photometry is derived from profile fitting, aperture correction is not needed. In principle, we could use a more realistic PRF such as the beam measured from maps of Neptune (a strong point-like source). However, we find that the Gaussian PRF is very good approximation of the real PRF and there is no bias in the flux density measurement for bright sources (see Section 3.3). For faint sources, confusion noise and instrument noise cause a systematic overestimation of the source flux (flux boosting) which is much larger than the photometric uncertainty caused by the Gaussian approximation of the PRF.

In principle, SF should extract a deeper source catalogue than SXT and return more accurate source positions and fluxes. However, when the instrument noise level is high (e.g. our Level 5 and Level 6 observations) or when the source profile is not well sampled, fewer sources would pass the correlation test and therefore SF would return a shallower catalogue than SXT.

Table 3. The average number of pixels and the average number of sources per segment.

Field	*N*(pixels)	*N*(sources)
L2 COSMOS	23.54	4.39
L3 Groth Strip	18.98	2.67
L4 UDS	15.90	3.21
L5 Lockman SWIRE	9.43	2.47
L6 ELAIS S1 SWIRE	8.31	2.26

2.3 The DESPHOT ALGORITHM

While SF is effective at identifying 'peaks' in crowded images, it is not optimized for accurate photometry in highly confused images such as those from *Herschel*-SPIRE. The primary reason is that it requires a large fraction of 'sky' pixels which are free from any source flux. Having a large number of 'sky' pixels allows the background to be accurately determined, and also for crowded clumps of sources to be isolated, i.e. sources may be blended together but are typically separated from other sources enough that placing an annulus around them is appropriate. In *Herschel*-SPIRE images, nearly every pixel is dominated by signal from sources, meaning that the background actually comes from blended sources which we are trying to extract.

To deal with these issues, we have developed a new algorithm for SPIRE source photometry, DESPHOT. Many of the details of the algorithm have been presented in Roseboom et al. (2010, 2012) in the context of cross-identifications with 24 μm and radio sources. However, a complete description is provided here for the sake of clarity. DESPHOT consists of the following conceptually distinct steps: map segmentation, source photometry, background estimation and noise estimation. We will explain each step in turn.

While in theory source photometry and background estimation do not require segmentation of the map, in practice it is often computationally infeasible to use the full image. We need to break the map into smaller segments that can then be processed independently without affecting the photometric accuracy. This is achieved by locating islands of high-SNR pixels enclosed by low-SNR pixels. The segmentation algorithm operates thus as follows.

(i) Locates all pixels with an SNR above some threshold (default value of SNR = 1).
(ii) Takes the first of these high-SNR pixel starting in the bottom-left corner of the image.
(iii) 'Grows' a region around this pixel by iteratively taking neighbouring high-SNR pixels.
(iv) Once there are no more high-SNR neighbours, jumps to the next high-SNR pixel and repeat from step (iii).

Each of these independent regions of high-SNR pixels is uniquely identified and will be processed separately by the source photometry component. Segment size changes with the depth of map, both in the number of pixels and in the number of sources in each segment. In Table 3, we list the average number of pixels and the average number of sources per segment in fields of different depths (from Level 2 to Level 6).

DESPHOT assumes that the map can be described as the sum of the flux densities from the n known sources

$$\boldsymbol{d} = \sum_{i=1}^{n} \boldsymbol{P}_i f_i + \boldsymbol{\delta}, \tag{1}$$

where $\boldsymbol{d}$ is the image, $\boldsymbol{P}_i$ the PRF for source i, $\boldsymbol{f}_i$ the flux density of source i and $\boldsymbol{\delta}$ some unknown noise term. A linear equation of this form will have a maximum likelihood solution of the form

$$\hat{\boldsymbol{f}} = (\mathbf{A}^{\mathrm{T}}\mathbf{N}_d{}^{-1}\mathbf{A})^{-1}\,\mathbf{A}^{\mathrm{T}}\mathbf{N}_d{}^{-1}\boldsymbol{d}, \tag{2}$$

where $\mathbf{A}$ is an m pixel by n source matrix which describes the PRF for each source and $\mathbf{N}_d = \langle \boldsymbol{\delta}\boldsymbol{\delta}^{\mathrm{T}} \rangle$ is the covariance matrix between the image pixels (assumed to be diagonal here). This equation can be solved directly, either by brute-force matrix inversion or via other linear methods (e.g. conjugate gradient methods) but this class of solution can create two significant problems. First, it ignores our prior knowledge that sources cannot have negative flux density. This is not just a conceptual annoyance, as in very degenerate cases (i.e. two sources very close together) the lack of a non-negative prior results in any symmetric pairing of positive and negative flux providing a good fit to the data. The second issue is overfitting. If we cannot provide a 100 per cent reliable input list, a simple linear solution does not have the power to discriminate between spurious and real sources and can result in the overall flux densities of real sources to be underestimated (as some flux is lost to spurious ones).

To solve both issues, Roseboom et al. (2012) introduced the non-negative, weighted, LASSO algorithm (Tibshirani 1996; Zou 2006; ter Braak et al. 2010). LASSO belongs to a class of methods known as 'active' set, in that it considers the solution vector (in this case the flux densities of the sources) to be either 'active', and to be optimized in the solution, or 'inactive', and set to zero. Basically, the algorithm is iterative. It starts with the solution flux vector set to zero. It then turns on a single source at a time (i.e. moves them to the active set) that has the largest partial derivative of the chi-squared χ^2 (i.e. the source that reduces the chi-squared the most). The non-negative prior means that the derivative is only considered for positive values of the flux, and the step taken in each iteration is the largest possible that keeps all the sources in the active set positive, and the activated source $\mathrm{d}\chi^2/\mathrm{d}f$ negative. This process continues until some tolerance level is reached. The active set approach allows the source photometry algorithm to remove sources which are not necessary to provide a good fit to the map, thus alleviating concerns about overfitting.

Next, we need to be able to estimate the level of background emission. SPIRE does not measure the absolute background level. As a result, the background level is unknown and all *Herschel*-SPIRE maps have been mean subtracted, i.e. the mean of the map is zero. In reality, the background in the final maps is composed of real but confused sources. For simplicity, we will model it as a constant background, and solve for this iteratively starting with the assumption that it is zero.

In DESPHOT, LASSO is used to solve equation (2) for each segment assuming no background. Then, the background, assumed to have a fixed value across the whole map, is estimated using the first-pass photometry values. Thus our model for the map is actually

$$\boldsymbol{d} = \sum_{i}^{n} \boldsymbol{P}_i f_i + B + \boldsymbol{\delta}, \tag{3}$$

where B is the fixed background. While a solution for the background could have been incorporated into equation (2), because we treat each map segment independently in the source photometry step it would not be possible to produce a single value for the entire map in this way. However, given a set of initial estimates for the fluxes f_i^0, we can estimate a value for the background B via

$$B = \boldsymbol{d} - \sum_{i}^{n} \boldsymbol{P}_i f_i^0. \tag{4}$$

Once the background value is established, the source photometry process is run again with the background subtracted. The flux density estimates from this second pass are the ones which enter the output catalogues.

Finally, we estimate the total noise on our sources, including the effect of confusion. As the use of LASSO and non-negative prior make the source photometry method non-linear, the most obvious way to estimate the noise would be a Monte Carlo simulation of the full DESPHOT algorithm. However, given that the typical processing time for an L5 field is ∼2 d on a large supercomputing node (∼20 cores and 256 GB of RAM), running simulations on this scale is not feasible. If we approximate the DESPHOT algorithm as linear, then we can get a lower limit on the noise via

$$\mathbf{N}_f \geq (\mathbf{A}^T \mathbf{N}_d^{-1} \mathbf{A})^{-1}. \quad (5)$$

However, this estimate only includes the instrumental noise (via $\mathbf{N}_d$) and the degeneracies between the input sources (via $\mathbf{A}$). In order to provide some estimate of the remaining confusion noise (i.e. the contaminating fluxes from sources not in the input), we use the global map statistics via the pixel intensity distribution. Specifically, we produce a single estimate of the residual confusion noise by measuring the standard deviation of pixels in the residual map, i.e. the SPIRE map with a reconstructed model using our final estimates of the background and source fluxes removed. The instrumental noise in the residual map must be removed to produce a clean estimate of the confusion noise. Thus, the confusion noise $\sigma_{\rm conf}$ is calculated by taking the standard deviation of the residual map pixels $\sigma_{\rm res}$ and removing the average instrumental noise in these pixels in quadrature, $\sigma^2_{\rm conf} = \sigma^2_{\rm res} - \sigma^2_{\rm pix}$, where $\sigma_{\rm pix}$ is calculated directly from the exposure time per pixel.[8] The total noise $\sigma_{\rm tot}$ for a point source is then calculated from both the instrumental noise (and confusion noise from the known sources), $\sigma_i = \sqrt{\rm diag((\mathbf{A}^T \mathbf{N}_d^{-1} \mathbf{A})^{-1})}$, and confusion noise from the unknown sources in the residual map $\sigma_{\rm conf}$ via $\sigma^2_{\rm tot} = \sigma^2_i + \sigma^2_{\rm conf}$.

3 PROPERTIES OF THE DR1 AND DR2 POINT SOURCE CATALOGUES

In this section, we will discuss the properties of HerMES DR1 and DR2 SXT, SF and SF250 catalogues with realistic end-to-end simulations designed to match real *Herschel*-SPIRE observations as well as the map-making and the point source extraction process.

3.1 End-to-end realistic simulations

To understand the characteristics of the point source catalogues, we need to make use of realistic simulations of *Herschel*-SPIRE observations. We give a brief summary of the steps taken to produce the simulations below.

(i) Generate a SPIRE input source catalogue based on the Béthermin et al. (2010) source count model with flux densities at 250, 350 and 500 μm.

(ii) Assign random coordinates (x, y) as well as clustered coordinates to the input catalogue generated from step (i) to make mock sky maps. The mock sky is then convolved with Gaussian-shaped PRFs to create mock SPIRE maps. The random mock sky is straightforward to generate by simply distributing the input sources randomly in the map. Source positions are the same in simulations at 250, 350 and 500 μm. Clustered coordinates are assigned as follows. First, we generate a single background density map with a power spectrum based on the clustering model fit in Viero et al. (2013) (both the one- and two-halo term, but not the Poisson term). Next, we draw positions weighted by the density map and assign source flux densities to each of the three simulated sky map bands for each position. The resulting simulated maps have sources correlated in position and colour, with power spectra resembling that of clustered dusty star-forming galaxies.

(iii) Scan the mock sky at 250, 350 and 500 μm and make time streams. At the same time, add realistic white and 1/f noise[9] to the simulated time streams (Pascale et al. 2011; Viero et al. 2013).

(iv) Run the time streams through the SMAP map-making pipeline, and then make final simulated maps which resemble the equivalent SMAP maps in the real observations. At the same time, it takes the input catalogue and map-specific header file and converts the catalogue coordinates from map pixel coordinates (x, y) to (RA, Dec.) while excluding those sources located outside the map.

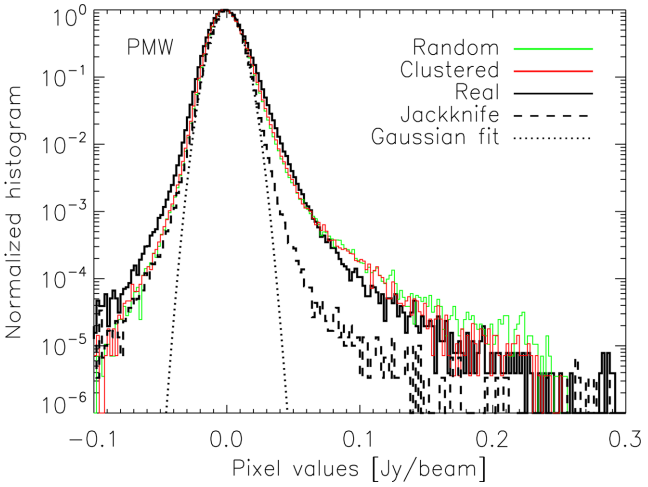

Figure 1. Histogram of pixel flux densities of the real map (black solid line), simulated maps (green line: random positions; red line: clustered positions) and jackknife noise map (black dashed line) of the Lockman the Spitzer Wide-area InfraRed Extragalactic survey (SWIRE) field at 350 μm (PMW). The black dotted line is a Gaussian fit to the pixel histogram of the jackknife noise map.

In total, we have simulated five different HerMES fields which are Lockman SWIRE, the Cosmological Evolution Survey field (COSMOS), the Ultra Deep Survey field (UDS), the European Large Area ISO Survey - South 1 field (ELAIS-S1) and the Extended Groth Strip field (EGROTH), covering a range of depth (Level 2 to Level 6). In Fig. 1, we plot the normalized pixel flux distribution in the real observation, simulated observations (both random and clustered) and jackknife noise map of the Lockman SWIRE field at 350 μm (PMW). The jackknife noise map is made by subtracting two independent maps of the same field using the first and second half of the data. Therefore, the jackknife difference map

[8] Nguyen et al. (2010) showed that the instrumental noise calculated from jackknife maps is consistent with the instrumental noise calculated based on exposure time.

[9] The noise levels are measured from the power spectrum of the difference map of the jackknife map-pairs in Viero et al. (2013). The instrumental noise consists of a scale-independent white noise term and 1/f noise. White noise dominates on angular scales $k_\theta \gtrsim 0.25$ arcmin^{-1}, while the 1/f noise term dominates on larger scales.

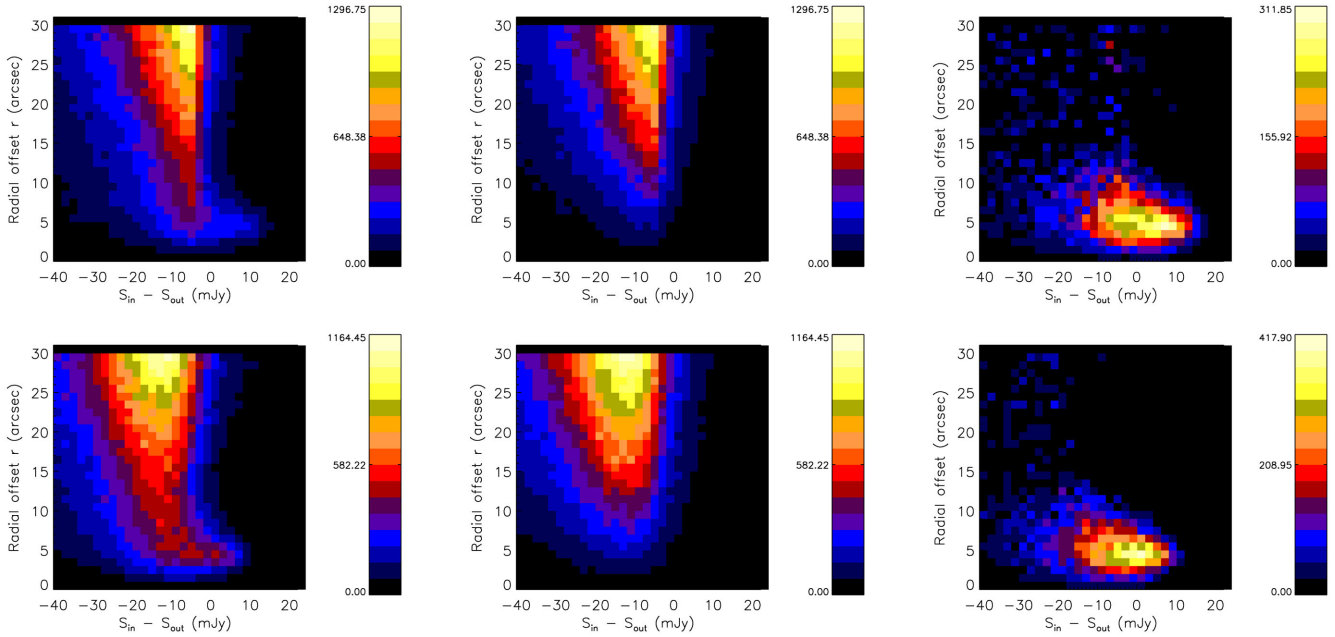

Figure 2. The 2D density distribution as a function of radial offset r and flux difference $S_{\rm in} - S_{\rm out}$ in the simulated unclustered COSMOS field at 250 μm (SXT: top panels; SF: bottom panels). The left-hand panels show the density distribution of all matches between the input and output catalogue. The middle panels show the density distribution of all matches between the input and the randomized output catalogue. The right-hand panels show the difference between the left and middle panels (note the changing colour scale) which can be approximated as the 2D density distribution of the real input–output matches.

should remove the sky signal and contain only the instrument noise. The overall shape of the histogram in the simulated maps matches very well to the real histogram. The non-Gaussianity of the real or simulated pixel histograms is due to the presence of point sources as well as the variation of the instrument noise level across the map (which results in a sum of Gaussian distributions). The latter is evident in the pixel histogram of the jackknife map.

In the following sections, we will mostly show results (e.g. positional and photometric accuracy) from the simulated COSMOS and Lockman SWIRE field. The other three fields exhibit similar overall trends.

3.2 Matching input with output

In the confusion-limited regime, matching the input catalogue with the output catalogue is far from trivial. On one hand, one detection in the output can result from blending of several input sources. On the other hand, one input source can sometimes contribute to more than one detection in the output.

We match the input truth list with the output source list using a likelihood ratio (LR) method similar to Chapin et al. (2011). For each input–output source pair, we calculate the LR, the ratio of probability of being a true match to probability of being a random association, based on the positional offset r and flux difference $\Delta S = S_{\rm in} - S_{\rm out}$,

$$LR(\Delta S, r) = \frac{q(\Delta S) f(r)}{2\pi r \rho(\Delta S)}, \quad (6)$$

where $f(r)$ is the probability distribution function (PDF) of the true matches between the input and output as a function of positional offset, $2\pi r$ is the positional distribution of the random matches (assuming a constant surface density of random matches), $q(\Delta S)$ is the PDF of the true matches as a function of flux difference and $\rho(\Delta S)$ is the PDF of the random matches as a function of flux difference.

In equation (6), we have assumed that the LR is separable in positional offset and flux difference. In other words, the flux difference distribution has no dependence on the positional offset and vice versa. To check whether this assumption is valid, we can look at the two-dimensional (2D) density distribution of real input–output matches in the radial offset r versus flux difference $\Delta S = S_{\rm in} - S_{\rm out}$ plane. In the left-hand panels in Fig. 2, we plot the 2D density distribution of all matches between the input and output catalogue in the unclustered COSMOS simulation at 250 μm, which include both the real and random matches between the input and output. In the middle panels in Fig. 2, we plot the density distribution of all matches between the input and randomized output catalogue,[10] which should only include random matches. The difference between the left and the middle panels, plotted in the right-hand panels in Fig. 2, can be approximated as the density distribution of the real input–output matches. We can see that the flux difference distribution at a given radial offset does not change significantly with which radial offset value we choose and similarly the radial offset distribution at a given flux difference does not change significantly with the flux difference either. Therefore, the separation of positional offset and flux difference in the LR calculation in equation (6) is justified. Simulations with randomly distributed input sources are used in Fig. 2, but the same conclusion that the distribution of positional offset and flux difference can be separated also holds for simulations with clustered input sources.

For the positional PDF of the real input–output matches, we assume a symmetric Gaussian distribution as a function of orthogonal positional coordinates. So, $f(r)$ follows a Rayleigh radial probability distribution,

$$f(r) = \frac{r}{\sigma_r^2} \exp(-r^2/2\sigma_r^2). \quad (7)$$

[10] The randomized output catalogue is generated by randomly disturbing the source positions and swapping flux densities between sources in the output list.

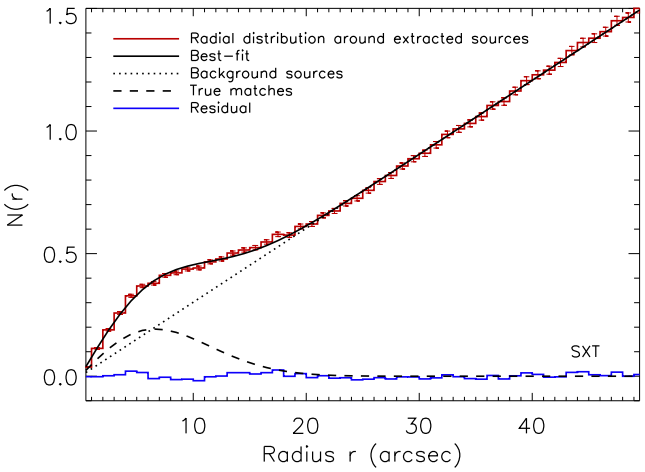

Figure 3. The radial distribution of positional offsets between extracted sources and input sources per extracted source (red line), the best-fitting model prediction (black solid line) and the difference between the two (blue line). The radial distribution of background input sources uncorrelated with the extracted source grows linearly with r. The radial distribution of true matches between the input and output follows a Rayleigh distribution. Note that in this plot we use the SXT 350 μm catalogue extracted from the unclustered simulation of the COSMOS field.

Table 4. The σ_r value in the Rayleigh radial probability distribution averaged over five different simulated fields at 250, 350 and 500 μm for SXT and SF catalogues. The top two rows correspond to simulations with randomly distributed input sources, while the bottom two rows correspond to simulations with clustered input sources. In all cases, the SF catalogues have slightly better positional accuracy than the SXT catalogues. By construction, SF250 source catalogues at 250, 350 and 500 μm have the same σ_r value as the SF catalogues at 250 μm.

Method	PSW (arcsec)	PMW (arcsec)	PLW (arcsec)
SXT (random)	5.3 ± 0.2	7.9 ± 0.7	12.7 ± 0.6
SF (random)	4.8 ± 0.2	7.2 ± 0.4	11.5 ± 0.5
SXT (clustered)	5.3 ± 0.2	7.7 ± 0.7	13.3 ± 0.8
SF (clustered)	4.8 ± 0.1	7.0 ± 0.3	11.8 ± 0.4

The positional distribution of random sources uncorrelated with the output sources follows a linear trend with the radial offset r assuming a constant surface density of background sources. In Fig. 3, we plot the histogram of radial offsets for all possible pairs between the input and output per output source within 50 arcsec. The histogram can be fitted by the sum of the true matches following a Rayleigh distribution and the random sources following a linear trend with r. Poisson errors in the histogram are used in the fitting procedure. We checked that bootstrap errors are very similar to the Poisson errors and do not change the fit. In Fig. 3, we use the SXT 350 μm catalogue extracted from the unclustered simulation of the COSMOS field. Similar trends are found in other simulations at other wavelengths. In Table 4, we list the best-fitting values and uncertainties for σ_r for SXT and SF catalogues averaged over all five simulated fields at 250, 350 and 500 μm, respectively. The difference between the clustered and unclustered simulations is very small at all wavelengths. By construction, SF250 source catalogues at 250, 350 and 500 μm have the same σ_r value as the SF catalogues at 250 μm. The SF catalogues have a smaller σ_r than the SXT catalogues at all wavelengths, which is expected as SF optimizes the source positions during the local fitting process.

Next, we need to determine the PDF of the true matches and random matches between the input and output as a function of flux difference, i.e. $q(\Delta S)$ and $\rho(\Delta S)$. It is straightforward to determine $\rho(\Delta S)$. We simply match the input list with the randomized output catalogue and derive the number of random matches as a function of ΔS. To determine $q(\Delta S)$, first we need to identify the search radius within which the SNR of the true matches is highest. Using the optimal search radii, we can then derive the histogram of the flux difference for all matches between the input and output. In Fig. 4, we plot the flux difference distribution of all matches between the input and output within the optical search radii, the flux difference distribution for all matches between the input and randomized output, and the difference between the two (i.e. $q(\Delta S)$) for the SXT, SF and SF250 source catalogues in the simulated unclustered COSMOS field. Errors on the flux difference distribution correspond to Poisson noise. We can see that for both SXT and SF catalogues, the peak of $q(\Delta S)$ shifts to lower values of ΔS from PSW to PLW, as a result of more severe blending as the beam size increases. The flux difference distribution of the real matches for the SF250 catalogues peaks much closer to zero compared to the SXT and SF catalogues at 350 and 500 μm. This is because the input SF catalogue extracted from the 250 μm map significantly reduces the level of confusion noise at 350 and 500 μm.

Having determined all the necessary positional and photometric PDFs, we can now calculate the LR of all matches between the input and output catalogue. But we still need to isolate the real matches between the input and output from the random matches. When the noise in the data is entirely due to instrumental effects, the probability that a detection is genuine (or spurious) can be estimated from the SNR of the source. However, in these *Herschel*-SPIRE data, the dominant source of noise is in general the confusion noise. So, the measurement of the flux density of any particular source is contaminated by the flux density of neighbouring sources. This means that the signal-to-(total) noise of a detection cannot be used in a straightforward way to give the probability that it is spurious. To circumvent this problem, we match the randomized output catalogue with the input catalogue and calculate the LR of each matched pair, which basically characterizes the LR distribution of spurious matches between the input and the output. As a result, we can derive the false identification rate[11] as a function of LR threshold. Finally, we select all matches between the input catalogue and the output catalogue with LR above the 10 per cent false identification rate as the true input–output matches.

3.3 Photometric accuracy and completeness

Having matched the input and output catalogue, we can look at the photometric accuracy of the extracted sources. In Fig. 5, we plot the output − input flux difference ($S_{\rm out} - S_{\rm in}$) to input flux ($S_{\rm in}$) ratio for extracted sources in different bins of input flux density at 250, 350 and 500 μm, for the three different types of source catalogues (SXT, SF and SF250) in the simulated unclustered COSMOS and Lockman SWIRE field. Simulations with clustered input sources give similar results. At the faint end ($<5\sigma$ limit), the output flux is generally larger than the input flux (the well-known flux-boosting effect) and the level of flux-boosting increases with decreasing input flux. At the bright end (flux densities $>5\sigma$ limit), the mean flux

[11] The false identification rate is defined as the ratio of the number of matches between the input and randomized output catalogue above a chosen LR threshold to the total number of matches.

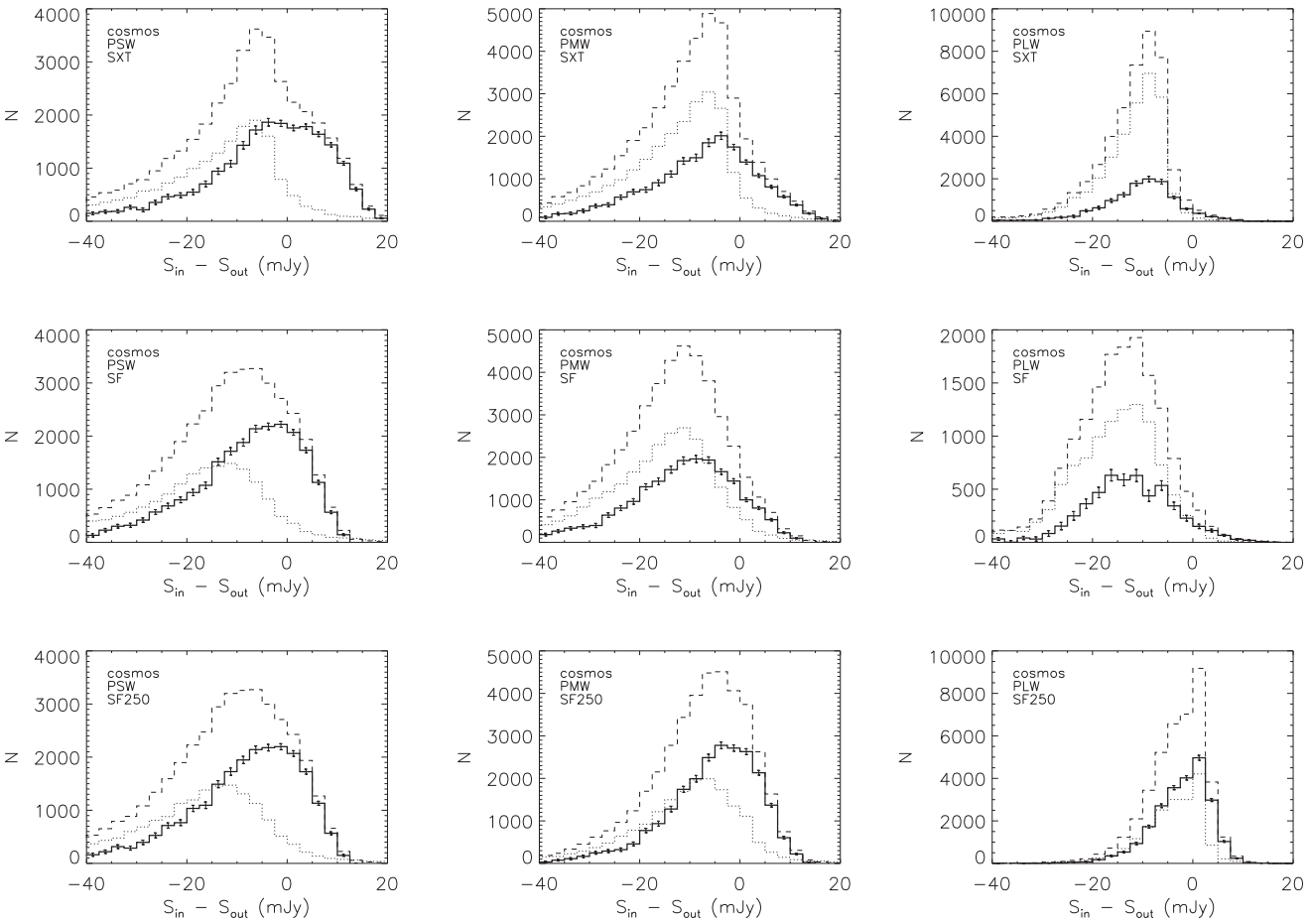

Figure 4. The flux difference distribution of all matches between the input and output (dashed histogram) in the simulated unclustered COSMOS field, between the input and randomized output (dotted histogram), and the difference between the two (solid histogram) for SXT (top panels), SF (middle panels) and SF250 (bottom panels) catalogues. Each column corresponds to a different band (left: 250 μm, PSW; middle: 350 μm, PSW; right: 500 μm, PLW).

difference to input flux ratio $(S_{\rm out} - S_{\rm in})/S_{\rm in}$ stays close to zero (the dashed line in Fig. 5) with an increasing scatter towards deceasing input flux. For each of the three types of source catalogues, the ratio $(S_{\rm out} - S_{\rm in})/S_{\rm in}$ deviates from the dashed line at a larger $S_{\rm in}$ value in the simulated Lockman SWIRE field than the COSMOS field, due to a higher level of instrument noise in the former (see Table 2). For the band-merged SF catalogues (SF250) extracted at the positions of SF 250 μm sources, the ratio $(S_{\rm out} - S_{\rm in})/S_{\rm in}$ deviates from the dashed line at a much smaller $S_{\rm in}$ value at 350 and 500 μm compared to the independent single-band SXT or SF catalogues, as a result of reduced confusion noise. We fit a geometric function of the form

$$\left(\frac{S_{\rm out} - S_{\rm in}}{S_{\rm in}}\right) = a_0 (S_{\rm in})^{a_1} + a_2 \qquad (8)$$

to describe the relation between the mean flux difference to input flux ratio as a function of input flux density. Here, a_1 is negative. So, as the input flux $S_{\rm in}$ increases to a very large number, the flux difference to input flux ratio asymptotes to a_2, $(S_{\rm out} - S_{\rm in})/S_{\rm in} = a_2$. a_1 describes how quickly the flux difference to input flux ratio rises (i.e. deviates from the asymptotic value a_2) as a function of decreasing $S_{\rm in}$ and a_0 is related to the input flux density at which $(S_{\rm out} - S_{\rm in})/S_{\rm in}$ starts to deviate from a_2. In other words, a_1 describes the rate of deviation and a_0 is related to the deviation point. In Table 5, we list the best-fitting values for the parameters in the geometric function at 250, 350 and 500 μm averaged over all five simulated fields, both clustered and unclustered. In all cases, a_2 is consistent with zero which means that for the bright input sources there is no systematic bias in the flux estimation in the SXT, SF and SF250 catalogues. We can see that averaged over different fields the rate of deviation a_2 is similar across different bands for the SXT and SF catalogues. The SF250 catalogues have a higher rate of deviation (i.e. steeper rise) and lower deviation point compared to the SXT and SF catalogues at 350 and 500 μm. Simulations with clustered input sources give in general similar results to the unclustered simulations but with a slightly higher deviation point. In Table 6, we list the interpolated output − input flux difference to input flux ratio at 250, 350 and 500 μm as a function of input flux based on the best-fitting geometric function in the unclustered simulation of the COSMOS, EROTH, UDS, ELAIS-S1 and Lockman SWIRE field. Clustered simulations give similar output − input flux difference to input flux ratio.

Completeness fraction is defined as the ratio of the number of input sources matched with sources in the output catalogue (i.e. detected input sources) to the total number of input sources in a given flux interval. As such, completeness fraction is defined as a function of input flux. After matching the input catalogue with the output catalogue as detailed in Section 3.2, it is straightforward to derive the completeness curve for each of our simulations. Input sources

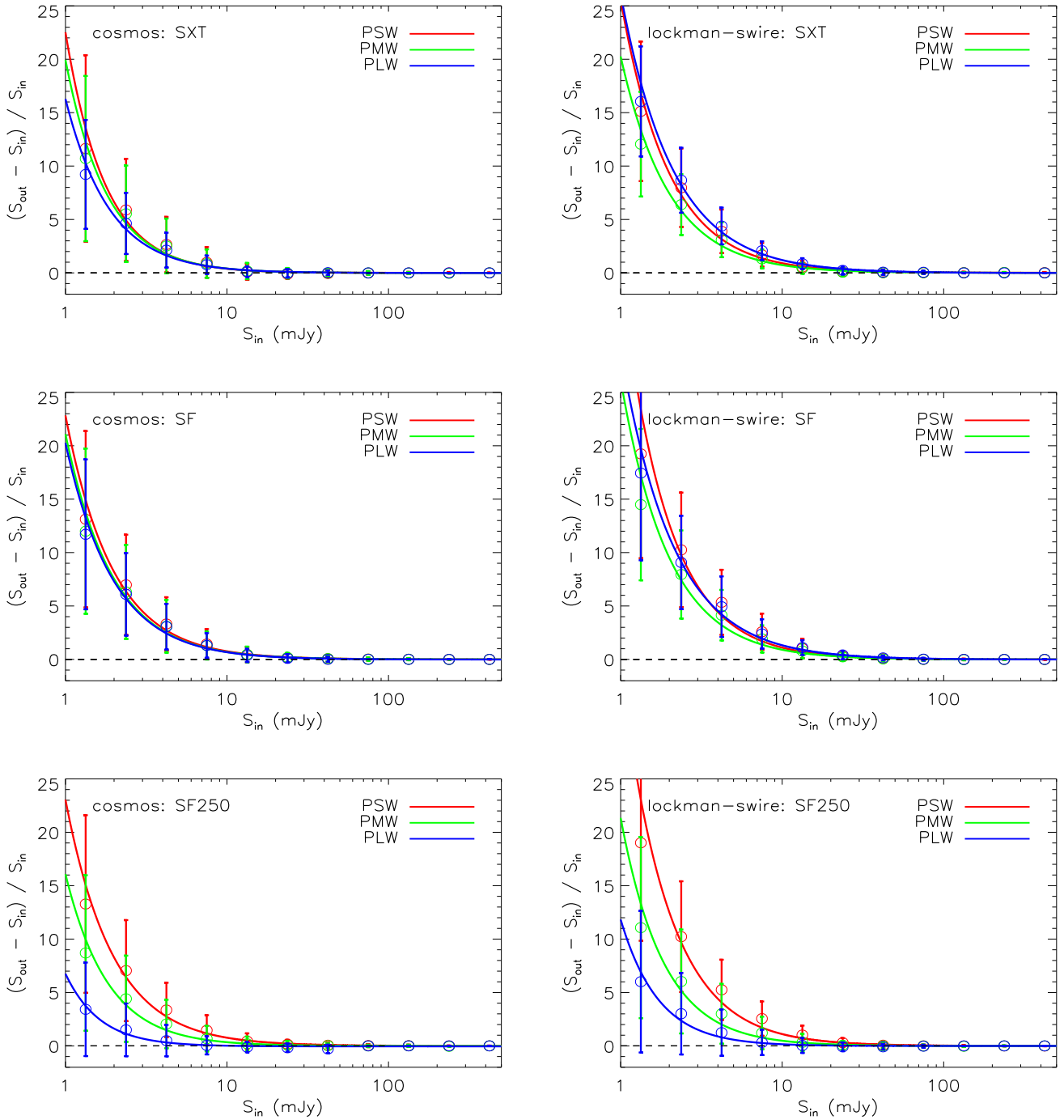

Figure 5. The flux difference (output flux − input flux) to input flux ratio as a function of input flux density at 250, 350 and 500 μm for the three different types of source catalogues (top: SXT; middle: SF; bottom: SF250). The horizontal dashed line corresponds to $S_{\rm out} = S_{\rm in}$. The left-hand column corresponds to the simulated unclustered COSMOS field and the right-hand column corresponds to the simulated unclustered Lockman SWIRE field. The curves are the best-fitting geometric functions (equation 8) which describe the ratio of output − input flux difference as a function of input flux density. The best-fitting coefficients averaged over all five simulated fields are listed in Table 5. Simulations with clustered input sources produce similar curves.

that are linked to more than one output source are counted only once to avoid double counting. Fig. 6 compares the completeness curves from SXT, SF and SF250 catalogues at 250, 350 and 500 μm in the simulated unclustered COSMOS and Lockman SWIRE field. In deep fields, SF catalogues are deeper than the SXT fields. In shallower fields, the opposite is true. A higher level of instrument noise in the shallow fields means that fewer sources would pass the correlation test between the source profile and the PRF in the SF source detection method. For a given source extraction method (SXT or SF), the completeness fraction at a given flux density drops as the level of instrument noise increases. Simulations with clustered sources produce similar completeness curves as a function of input

Table 5. The best-fitting value and scatter for the parameters in the geometric function (equation 8) which describes the ratio of output − input flux difference to input flux as a function of input flux density averaged over five different simulated fields at 250, 350 and 500 μm. The top three rows correspond to simulations with randomly distributed input sources, while the bottom three rows correspond to simulations with clustered input sources. The difference between the clustered and unclustered simulations is small.

Method	a_0^{250}	a_0^{350}	a_0^{500}	a_1^{250}	a_1^{350}	a_1^{500}	a_2^{250}	a_2^{350}	a_2^{500}
SXT (random)	20.5(4.4)	16.9(3.3)	19.7(4.7)	−1.6(0.1)	−1.5(0.1)	−1.4(0.1)	0.0(0.0)	0.0(0.0)	0.0(0.0)
SF (random)	25.6(7.2)	20.5(4.3)	22.3(4.7)	−1.5(0.0)	−1.5(0.0)	−1.4(0.1)	0.0(0.0)	0.0(0.0)	0.0(0.0)
SF250 (random)	25.6(7.2)	17.2(3.1)	8.7(2.2)	−1.5(0.0)	−1.7(0.1)	−2.0(0.2)	0.0(0.0)	0.0(0.0)	0.0(0.0)
SXT (clustered)	17.9(9.1)	21.0(4.5)	21.4(5.4)	−1.4(0.4)	−1.7(0.4)	−1.4(0.1)	0.0(0.0)	0.0(0.0)	0.0(0.0)
SF (clustered)	26.9(7.1)	22.3(5.5)	22.9(6.3)	−1.6(0.1)	−1.5(0.1)	−1.4(0.1)	0.0(0.0)	0.0(0.0)	0.0(0.0)
SF250 (clustered)	26.9(7.1)	18.7(3.6)	9.3(2.7)	−1.6(0.1)	−1.7(0.1)	−1.9(0.1)	0.0(0.0)	0.0(0.0)	0.0(0.0)

Table 6. The output − input flux difference to input flux ratio at 250, 350 and 500 μm for SXT, SF and SF250 catalogues extracted from unclustered simulations. For each catalogue, we give the interpolated output − input flux difference to input flux ratio at a given flux node based on the best-fitting geometric function (equation 8) in the simulated COSMOS (C), EGROTH (EG), UDS (U), ELAIS-S1 (EL) and Lockman-SWIRE (L) field. Clustered simulations give similar output − input flux difference to input flux ratios.

S_{250} (mJy)	$\frac{S_{out}-S_{in}}{S_{in}}$ (SXT; random)					$\frac{S_{out}-S_{in}}{S_{in}}$ (SF; random)				
	C	EG	U	EL	L	C	EG	U	EL	L
5	1.32	1.27	1.29	2.00	2.47	2.11	1.56	1.51	2.51	3.16
10	0.39	0.43	0.44	0.71	0.90	0.76	0.52	0.50	0.86	1.10
20	0.11	0.15	0.15	0.25	0.33	0.27	0.18	0.17	0.30	0.38
40	0.03	0.06	0.06	0.09	0.13	0.10	0.06	0.06	0.10	0.13
80	0.01	0.02	0.02	0.04	0.05	0.03	0.02	0.02	0.03	0.04
160	0.00	0.01	0.01	0.02	0.02	0.01	0.01	0.01	0.01	0.01

S_{350} (mJy)	$\frac{S_{out}-S_{in}}{S_{in}}$ (SXT; random)					$\frac{S_{out}-S_{in}}{S_{in}}$ (SF; random)					$\frac{S_{out}-S_{in}}{S_{in}}$ (SF250; random)				
	C	EG	U	EL	L	C	EG	U	EL	L	C	EG	U	EL	L
5	1.31	1.20	1.28	1.64	1.98	1.93	1.34	1.30	2.03	2.50	1.11	0.76	0.74	1.31	1.52
10	0.40	0.41	0.48	0.60	0.73	0.69	0.45	0.45	0.72	0.91	0.35	0.21	0.20	0.41	0.48
20	0.12	0.14	0.18	0.22	0.27	0.25	0.15	0.15	0.25	0.33	0.11	0.05	0.05	0.12	0.15
40	0.03	0.05	0.07	0.08	0.10	0.09	0.05	0.05	0.09	0.12	0.03	0.01	0.01	0.04	0.05
80	0.01	0.01	0.03	0.03	0.04	0.03	0.01	0.02	0.03	0.04	0.01	0.00	0.00	0.01	0.01
160	0.00	0.00	0.02	0.01	0.01	0.01	0.00	0.00	0.01	0.01	0.00	0.00	0.00	0.00	0.00

S_{500} (mJy)	$\frac{S_{out}-S_{in}}{S_{in}}$ (SXT; random)					$\frac{S_{out}-S_{in}}{S_{in}}$ (SF; random)					$\frac{S_{out}-S_{in}}{S_{in}}$ (SF250; random)				
	C	EG	U	EL	L	C	EG	U	EL	L	C	EG	U	EL	L
5	1.23	1.87	1.58	2.46	3.04	1.89	1.89	1.82	2.64	3.36	0.21	0.20	0.29	0.51	0.58
10	0.40	0.71	0.60	0.94	1.20	0.67	0.72	0.65	0.99	1.32	0.02	0.04	0.07	0.14	0.15
20	0.13	0.27	0.23	0.36	0.47	0.23	0.26	0.23	0.37	0.51	−0.0	0.00	0.02	0.04	0.04
40	0.04	0.10	0.09	0.13	0.18	0.08	0.09	0.08	0.13	0.20	−0.0	−0.0	0.00	0.01	0.00
80	0.01	0.04	0.03	0.05	0.06	0.02	0.02	0.03	0.05	0.07	−0.0	−0.0	0.00	0.00	0.00
160	0.00	0.01	0.01	0.01	0.02	0.00	−0.0	0.01	0.01	0.02	−0.0	−0.0	0.00	0.00	−0.0

flux. To fit the completeness fraction as a function of input flux density, we can use the generalized logistic function[12]

$$C(S_{in}) = A + \frac{K - A}{(1 + Q\exp(-(S_{in} - M)/B))^N}. \quad (9)$$

We can set $A = 0$ (the lower asymptote) and $K = 1$ (the upper asymptote) as the completeness fraction C should approach 100 and 0 per cent when S_{in} goes to very large and very small values, respectively. In Table 7, we list the interpolated completeness level at 250, 350 and 500 μm as a function of input flux based on the best-fitting generalized logistic function in the unclustered simulation of the COSMOS, EROTH, UDS, ELAIS-S1 and Lockman SWIRE field. Clustered simulations give similar results.

[12] The (generalized) logistic function is a type of sigmoid function ('S'-shaped function), often used to model population growth. It shows initial exponential growth when the independent variable is small, followed by slower growth with increasing values of the independent variable, and eventually reaches saturation point when the independent variable is large.

4 EXTENDED SOURCES

Our source detection and extraction methods assume point sources. Objects that are extended on the scale of the SPIRE beam (see Fig. 7) are not expected to be accurately represented. The SXT detection and extraction will lead to inaccurate flux estimation (probably biased low) and very large objects may be misidentified as multiple point sources. Similarly, SF will underestimate fluxes and is expected to break even modestly extended object into multiple point sources. We have thus flagged detections as extended using the following criteria.

We have cross-matched all SPIRE detections with their nearest (within 30 arcsec) counterpart in the 2MASS Extended Source Catalog (XSC; Jarrett et al. 2000). Any detection matched to a counterpart with a K fiducial Kron elliptical aperture semimajor

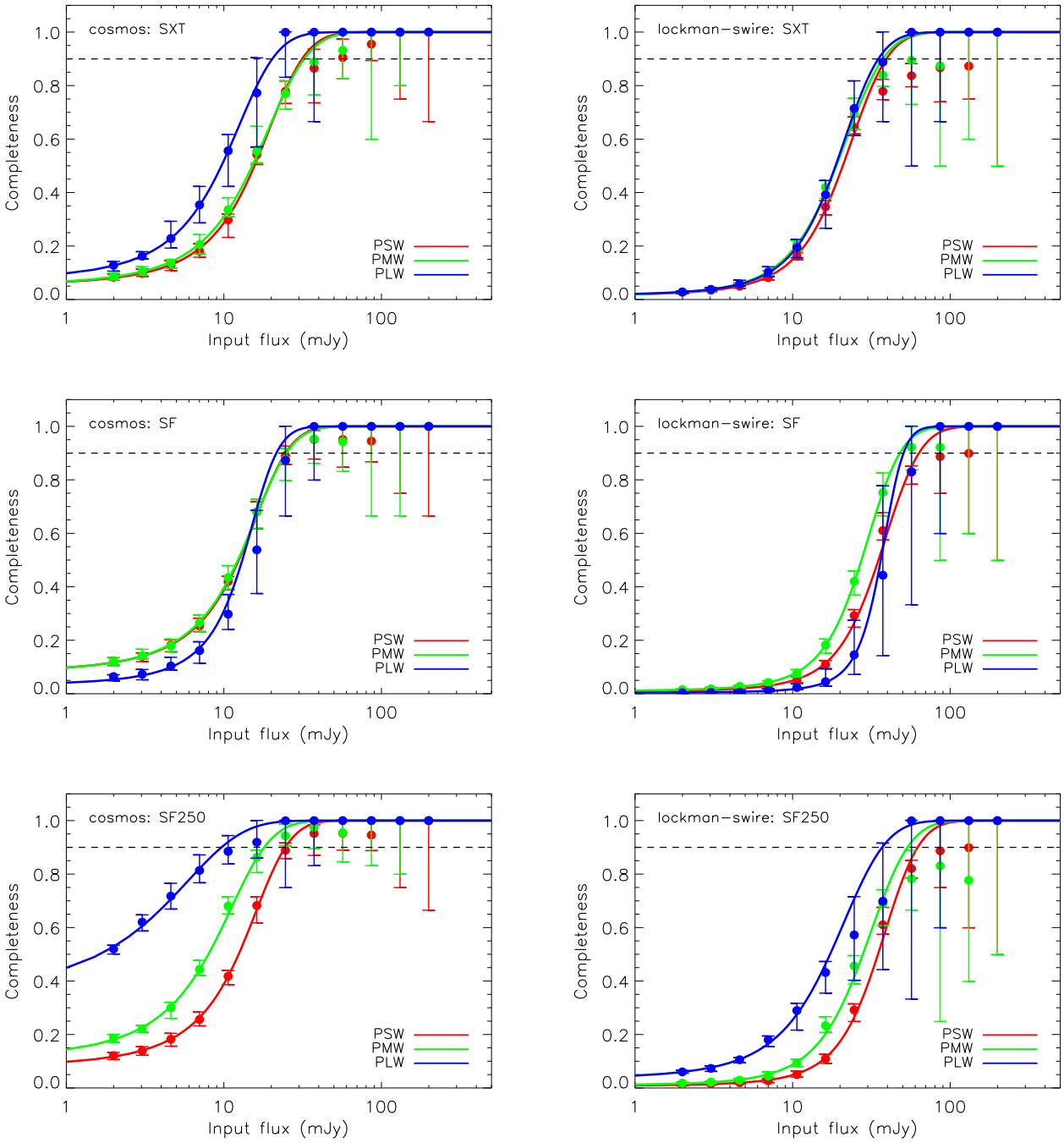

Figure 6. The completeness fraction as a function of input flux density at 250, 350 and 500 μm for the three different types of source catalogues (top: SXT; middle: SF; bottom: SF250). The horizontal dashed line marks the 90 per cent completeness level. The left-hand column corresponds to the simulated unclustered COSMOS field and the right-hand column corresponds to the simulated unclustered Lockman SWIRE field. The curves are the best-fitting generalized logistic functions to describe the completeness ratio as a function of input flux density. Simulations with clustered input sources produce similar completeness curves.

axis >9 arcsec is flagged as extended. We have then cross-matched all SPIRE detections with sources in the new catalogue of principal galaxies (PGC2003) which constitutes the HyperLeda data base[13] (Paturel et al. 2003). A counterpart is identified where a 30 arcsec radius circle around the SPIRE position intersects with the 25 *B*-mag arcsec^{-2} isophotal ellipse. Any detection with a counterpart with diameter at this isophot (D25) >18 arcsec is flagged as extended. These scales were chosen as they correspond to the FWHM

[13] PGC2003 contains about one million confirmed galaxies flux limited to ∼18 *B*-mag. HyperLeda (http://leda.univ-lyon1.fr) provides the richest catalogue of homogeneous parameters of galaxies for the largest available sample, and is thus useful when trying to estimate galaxy sizes in an homogeneous manner.

Table 7. The completeness fraction at 250, 350 and 500 μm for SXT, SF and SF250 catalogues extracted from unclustered simulations. For each catalogue, we give the interpolated completeness level at a given flux node based on the best-fitting generalized logistic function (equation 9) in the simulated COSMOS (C), EGROTH (EG), UDS (U), ELAIS-S1 (EL) and Lockman-SWIRE (L) field. Clustered simulations give similar completeness fractions.

S_{250} (mJy)	Comp (SXT; random)					Comp (SF; random)				
	C	EG	U	EL	L	C	EG	U	EL	L
5	0.14	0.11	0.12	0.08	0.06	0.19	0.13	0.13	0.04	0.02
10	0.29	0.28	0.31	0.21	0.15	0.39	0.32	0.34	0.09	0.05
20	0.66	0.66	0.71	0.59	0.47	0.80	0.81	0.79	0.36	0.17
40	0.97	0.96	0.97	0.95	0.91	0.99	1.00	0.99	0.91	0.60
80	1.00	1.00	1.00	1.00	1.00	1.00	1.00	1.00	1.00	0.97
160	1.00	1.00	1.00	1.00	1.00	1.00	1.00	1.00	1.00	1.00

S_{350} (mJy)	Comp (SXT; random)					Comp (SF; random)					Comp (SF250; random)				
	C	EG	U	EL	L	C	EG	U	EL	L	C	EG	U	EL	L
5	0.15	0.09	0.10	0.08	0.07	0.20	0.15	0.15	0.05	0.03	0.33	0.21	0.22	0.07	0.03
10	0.31	0.22	0.25	0.22	0.18	0.40	0.37	0.38	0.13	0.07	0.61	0.49	0.51	0.18	0.09
20	0.66	0.68	0.61	0.59	0.54	0.80	0.82	0.79	0.46	0.28	0.93	0.90	0.88	0.56	0.30
40	0.96	0.99	0.94	0.94	0.92	0.99	0.99	0.99	0.93	0.80	1.00	1.00	1.00	0.96	0.75
80	1.00	1.00	1.00	1.00	1.00	1.00	1.00	1.00	1.00	1.00	1.00	1.00	1.00	1.00	0.99
160	1.00	1.00	1.00	1.00	1.00	1.00	1.00	1.00	1.00	1.00	1.00	1.00	1.00	1.00	1.00

S_{500} (mJy)	Comp (SXT; random)					Comp (SF; random)					Comp (SF250; random)				
	C	EG	U	EL	L	C	EG	U	EL	L	C	EG	U	EL	L
5	0.25	0.16	0.15	0.09	0.06	0.11	0.07	0.09	0.02	0.01	0.73	0.49	0.52	0.23	0.12
10	0.52	0.45	0.39	0.26	0.18	0.31	0.28	0.25	0.05	0.02	0.91	0.78	0.76	0.45	0.25
20	0.89	0.94	0.84	0.73	0.55	0.86	0.90	0.75	0.29	0.07	0.99	0.98	0.96	0.79	0.58
40	1.00	1.00	1.00	0.99	0.94	1.00	1.00	0.99	0.97	0.64	1.00	1.00	1.00	0.98	0.92
80	1.00	1.00	1.00	1.00	1.00	1.00	1.00	1.00	1.00	1.00	1.00	1.00	1.00	1.00	1.00
160	1.00	1.00	1.00	1.00	1.00	1.00	1.00	1.00	1.00	1.00	1.00	1.00	1.00	1.00	1.00

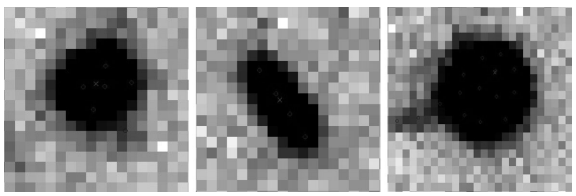

Figure 7. Examples of extended sources in the Lockman SWIRE region.

of the SPIRE beam at 250 μm and could conservatively reproduce other classifications, i.e. all objects which we have identified as bright and extended or nearby by eye and clusters of four or more SF detections. This procedure flags 6169 SPIRE detections as extended. The number of detections is much larger than the number of extended galaxies they represent as the detections include objects detected by either of the two techniques, in any SPIRE band, and multiple components of a single galaxy. Some optically extended sources might appear as compact point sources relative to the SPIRE beams (e.g. Smith et al. 2012). These sources will be removed as extended sources using our methods.

Another test which informed and supplemented our flagging method was an analysis of SPIRE-detected sources with a poor PRF fit at the position of the *Spitzer* 24 μm position. Visual inspection revealed that those detections appeared to be extended. Most of these (∼90 per cent) have already been flagged as extended by the methods described above. The remaining 10 per cent (200 detections) were then also flagged as extended which brings the total number of extended sources to 6369. However, this additional safety check has only been done in regions with *Spitzer* 24 μm data.

Infrared-bright but optically faint extended sources (Cortese et al. 2010) will be difficult to remove by cross-matching to the 2MASS XSC or the PGC2003 catalogue. However, the last method described in this section which uses the goodness of fit of the SPIRE-detected sources by the PRF should be able to remove those sources.

5 CONCLUSIONS AND DISCUSSIONS

In this paper, we present independent single-band SXT and SF point source catalogues as well as band-merged SF catalogues (SF250) extracted at the positions of the SF 250 μm sources released in HerMES DR1 and DR2. For SF and SF250 catalogues, we use our own code DESPHOT for accurate photometry. End-to-end simulations with realistic number counts and clustering behaviour matched to the observed counts and power spectra of the SPIRE sources are generated to characterize the basic properties of the source catalogues.

We use an LR method to match the simulated input sources with the output sources. The matched input and output catalogues are estimated to have a false identification rate of 10 per cent. We find that the positional distribution of real matches between the input and output peaks at approximately 5, 8 and 13 arcsec at 250, 350 and 500 μm for SXT catalogues, and approximately at 5, 7 and 12 arcsec at 250, 350 and 500 μm for SF catalogues. Both source extraction methods (SXT and SF) return unbiased flux measurement for bright sources at $>5\sigma$ (with respect to the total noise including confusion noise and instrument noise). The overall calibration uncertainty is 7 per cent. For faint sources, the output flux systematically overestimates the input flux and the level of flux-boosting (the output − input flux difference to input flux ratio) increases rapidly with decreasing input flux. At a given input flux, the level of flux boosting also increases with the level of instrument noise. The completeness fraction as function of input flux is also characterized for the three different types of source catalogues based on our simulations. In the deep fields, SF catalogues are generally

deeper than the SXT catalogues. In the shallower fields with a higher instrument noise level, the opposite is true. By construction, the SF250 catalogues are deeper than the independent SF catalogues at 350 and 500 μm but it will miss sources which are only detected at 350 and/or 500 μm. Fitting formulae for the positional accuracy, photometric accuracy and completeness fraction are given in the paper. We find that the impact of source clustering on the positional and photometric accuracy as well as the completeness fraction is small.

The Neptune radiative model has changed since the HerMES DR2 catalogues were made public. This resulted in photometric changes of a few per cent. We advise users to apply flux correction factors of 1.0253, 1.0250 and 1.0125 at 250, 350 and 500 μm, respectively, to sources in the released catalogues.

ACKNOWLEDGEMENTS

LW is supported by UK's Science and Technology Facilities Council grant ST/F002858/1 and an ERC StG grant (DEGAS-259586). The data presented in this paper will be released through the HeDaM (hedam.lam.fr/HerMES). SPIRE has been developed by a Consortium of Institutes led by Cardiff Univ. (UK) and including Univ. Lethbridge (Canada); NAOC (China); CEA, LAM (France); IFSI, Univ. Padua (Italy); IAC (Spain); Stockholm Observatory (Sweden); Imperial College London, RAL, UCL-MSSL, UKATC, Univ. Sussex (UK); Caltech, JPL, NHSC, Univ. Colorado (USA). This development has been supported by national funding agencies: CSA (Canada); NAOC (China); CEA, CNES, CNRS (France); ASI (Italy); MCINN (Spain); SNSB (Sweden); STFC (UK); and NASA (USA).

REFERENCES

Béthermin M., Dole H., Beelen A., Aussel H., 2010, A&A, 512, A78
Béthermin M. et al., 2012, A&A, 542, A58
Chapin E. L. et al., 2011, MNRAS, 411, 505
Cortese L., Bendo G. J., Isaak K. G., Davies J. I., Kent B. R., 2010, MNRAS, 403, L26
Diolaiti E., Bendinelli O., Bonaccini D., Close L., Currie D., Parmeggiani G., 2000, A&AS, 147, 335
Dowell C. D. et al., 2010, Proc. SPIE, 7731, 773136
Glenn J. et al., 2010, MNRAS, 409, 109
Griffin M. J. et al., 2010, A&A, 518, L3
Hobson M. P., Rocha G., Savage R. S., 2010, Bayesian Methods in Cosmology. Cambridge Univ. Press, Cambridge, p. 167
Jarrett T. H., Chester T., Cutri R., Schneider S., Skrutskie M., Huchra J. P., 2000, AJ, 119, 2498
Levenson L. et al., 2010, MNRAS, 409, 83
Nguyen H. T. et al., 2010, A&A, 518, L5
Oliver S. J. et al., 2010, A&A, 518, L21
Oliver S. J. et al., 2012, MNRAS, 424, 1614
Ott S., 2010, in Mizumoto Y., Morita K.-I., Ohishi M., eds, ASP Conf. Ser. Vol. 434, Astronomical Data Analysis Software and Systems XIX. Astron. Soc. Pac., San Francisco, p. 139
Pascale E. et al., 2011, MNRAS, 415, 911
Paturel G., Petit C., Prugniel P., Theureau G., Rousseau J., Brouty M., Dubois P., Cambrésy L., 2003, A&A, 412, 45
Pilbratt G. L. et al., 2010, A&A, 518, L1
Poglitsch A. et al., 2010, A&A, 518, L2
Roehlly Y., Buat V., Heinis S., Moreau C., Gimenez S., 2011, in Evans I. N., Accomazzi A., Mink D. J., Rots A. H., eds, ASP Conf. Ser. Vol. 442, HeDaM: The Herschel Database in Marseille. Astron. Soc. Pac., San Francisco, p. 25
Roseboom I. G. et al., 2010, MNRAS, 409, 48
Roseboom I. G. et al., 2012, MNRAS, 419, 2758
Savage R. S., Oliver S., 2007, ApJ, 661, 1339
Smith A. J. et al., 2011, MNRAS, 419, 377
Smith M. W. L. et al., 2012, ApJ, 748, 123
Swinyard B. M. et al., 2010, A&A, 518, L4
ter Braak C. J. F., Boer M. P., Totir L. R., Winkler C. R., Smith O. S., Bink M. C. A. M., 2010, Genetics, 185, 1045
Tibshirani R., 1996, J. R. Stat. Soc. B, 58, 267
Viero M. P. et al., 2013, ApJ, 772, 77
Zou H., 2006, J. Am. Stat. Assoc., 101, 1418

This paper has been typeset from a TEX/LATEX file prepared by the author.